Article

Neuron

Visual Areas Exert Feedforward and Feedback Influences through Distinct Frequency Channels

Highlights

- Influences among visual areas are dominated by theta, beta, and gamma-band rhythms
- Theta and gamma rhythms subserve feedforward, the beta rhythm feedback influences
- Frequency-specific directed influences constitute a functional hierarchy
- Functional hierarchy changes with behavioral context, especially for frontal areas

Authors

André Moraes Bastos, Julien Vezoli, ..., Henry Kennedy, Pascal Fries

Correspondence

pascal.fries@esi-frankfurt.de

In Brief

Primate visual areas are arranged in an anatomical hierarchy. Bastos et al. show that bottom-up signaling utilizes theta and gamma rhythms, and top-down signaling the beta rhythm. This differential signaling constrains a functional hierarchy that can change dynamically.

Bastos et al., 2015, Neuron *85*, 1–12
January 21, 2015
http://dx.doi.org/10.1016/j.neuron.2014.12.018

CellPress

Please cite this article in press as: Bastos et al., Visual Areas Exert Feedforward and Feedback Influences through Distinct Frequency Channels, Neuron (2015), http://dx.doi.org/10.1016/j.neuron.2014.12.018

Neuron
Article

Visual Areas Exert Feedforward and Feedback Influences through Distinct Frequency Channels

André Moraes Bastos,[1,2,3,8] Julien Vezoli,[1,8] Conrado Arturo Bosman,[2,4,8] Jan-Mathijs Schoffelen,[2,9] Robert Oostenveld,[2] Jarrod Robert Dowdall,[1] Peter De Weerd,[2,5] Henry Kennedy,[6,7] and Pascal Fries[1,2,*]

[1]Ernst Strüngmann Institute (ESI) for Neuroscience in Cooperation with Max Planck Society, Deutschordenstraße 46, 60528 Frankfurt, Germany

[2]Donders Institute for Brain, Cognition and Behaviour, Radboud University Nijmegen, Kapittelweg 29, 6525 EN Nijmegen, Netherlands

[3]Center for Neuroscience and Center for Mind and Brain, University of California, Davis, 1544 Newton Court, Davis, CA 95618, USA

[4]Swammerdam Institute for Life Sciences, Center for Neuroscience, Faculty of Science, University of Amsterdam, Sciencepark 904, 1098 XH Amsterdam, Netherlands

[5]Department of Neurocognition, University of Maastricht, Universiteitssingel 40, 6229 ER Maastricht, Netherlands

[6]Stem Cell and Brain Research Institute, INSERM U846, 18 Avenue Doyen Lépine, 69675 Bron, France

[7]Université de Lyon, 37 rue du Repos, 69361 Lyon, France

[8]Co-first authors

[9]Present address: Max Planck Institute for Psycholinguistics, Wundtlaan 1, 6525 XD Nijmegen, Netherlands

*Correspondence: pascal.fries@esi-frankfurt.de

http://dx.doi.org/10.1016/j.neuron.2014.12.018

SUMMARY

Visual cortical areas subserve cognitive functions by interacting in both feedforward and feedback directions. While feedforward influences convey sensory signals, feedback influences modulate feedforward signaling according to the current behavioral context. We investigated whether these interareal influences are subserved differentially by rhythmic synchronization. We correlated frequency-specific directed influences among 28 pairs of visual areas with anatomical metrics of the feedforward or feedback character of the respective interareal projections. This revealed that in the primate visual system, feedforward influences are carried by theta-band (~4 Hz) and gamma-band (~60–80 Hz) synchronization, and feedback influences by beta-band (~14–18 Hz) synchronization. The functional directed influences constrain a functional hierarchy similar to the anatomical hierarchy, but exhibiting task-dependent dynamic changes in particular with regard to the hierarchical positions of frontal areas. Our results demonstrate that feedforward and feedback signaling use distinct frequency channels, suggesting that they subserve differential communication requirements.

INTRODUCTION

Many aspects of cognitive performance can only be explained through the concept of feedback influences. For example, reaction times are shortened when stimulus locations are precued and attention can be predirected, an effect that cannot be explained if only feedforward input is considered (Posner et al., 1980). Numerous neurophysiological studies have demonstrated the effects of feedback influences on neuronal activity (Moran and Desimone, 1985), yet the mechanisms through which feedback influences are exerted remain elusive. Anatomical studies show that structural connections in the feedforward direction, i.e., from the primary sensory areas to higher order areas, are reciprocated by connections in the feedback direction (Felleman and Van Essen, 1991; Markov et al., 2014b). In addition, it is well established that feedforward and feedback connections follow a characteristic pattern with regard to cortical layers. Feedforward connections target the granular layer (Felleman and Van Essen, 1991); they originate preferentially in supragranular layers, and this preference is stronger for projections traversing more hierarchical levels, i.e., it is quantitatively related to the hierarchical distance (Markov et al., 2014b). Feedback connections avoid targeting the granular layer (Felleman and Van Essen, 1991); they originate preferentially in the infragranular layers, and again, this preference is stronger for projections traversing more hierarchical levels and is thereby quantitatively related to hierarchical distance (Markov et al., 2014b). These asymmetries have been used to arrange the visual cortical areas into a hierarchy (Felleman and Van Essen, 1991; Markov et al., 2014b), which has influenced many theories of cognition and brain function (Bastos et al., 2012; Dehaene et al., 1998; Lamme and Roelfsema, 2000; Mesulam, 1998).

Recent studies have documented a neurophysiological asymmetry between the layers of visual cortex. While supragranular layers show local gamma-band synchronization, infragranular layers show local alpha/beta-band synchronization (Buffalo et al., 2011; Roberts et al., 2013; Xing et al., 2012). Local rhythmic synchronization can lead to interareal synchronization (Bosman et al., 2012; Buschman and Miller, 2007; Gregoriou et al., 2009; Salazar et al., 2012), which has been proposed as a mechanism of effective interareal interaction (Bosman et al., 2012; Fries, 2005; Womelsdorf et al., 2007). Given that supragranular layers primarily send feedforward projections and infragranular layers primarily feedback projections, this leads to the

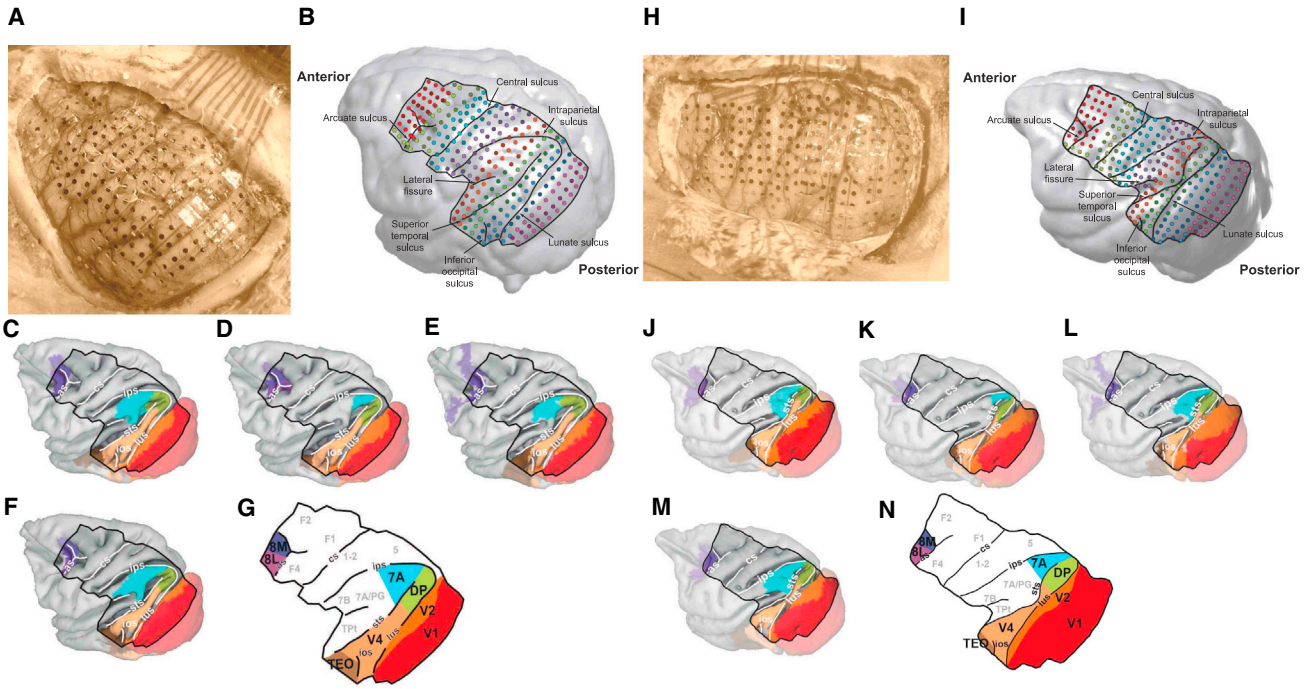

Figure 1. ECoG Electrode Distribution and Coregistration with Atlases

(A) Intraoperative photograph of the brain of monkey 1 after placement of the ECoG grid.

(B) Rendering of the brain of monkey 1 based on structural MRI scans. Lines indicate the boundary of the covered brain region and the major sulci, and dots indicate the 252 subdural electrodes (electrode color refers to headstage number, see Experimental Procedures for details).

(C–F) Midthickness surface of the brain coregistered in Caret (http://www.nitrc.org/projects/caret/) to the Macaque.F99 space and thereby to the following atlases: (C), "Felleman-VE all (1991)"; (D), "PHT 00 (PaxinosEtAl)"; (E), "Markov-CC10"; (F), "Markov-CC12." The visual areas that were covered by the ECoG grid are highlighted.

(G) Parcellation of ECoG-covered regions into cortical areas.

(H–N) Same as (A)–(G), but for monkey 2.

hypothesis that interareal synchronization in the gamma-frequency band might mediate feedforward influences, and interareal synchronization in the beta-frequency band might mediate feedback influences (Bastos et al., 2012; van Kerkoerle et al., 2014; Wang, 2010).

RESULTS

To test this prediction, we recorded local field potentials (LFPs) from electrocorticography (ECoG) grids implanted onto the left hemispheres of two macaque monkeys (Figures 1A, 1B, 1H, and 1I) performing a visuospatial attention task (Figure 2 and Experimental Procedures) (Bosman et al., 2012; Brunet et al., 2013, 2014; Rubehn et al., 2009). The ECoG grid covered eight visual areas: V1, V2, V4, TEO, DP, 7A, 8L, and 8M (lateral and medial parts of area 8/FEF). The 252 electrodes were assigned to cortical areas by coregistering intraoperative photographs with several macaque brain atlases (Van Essen, 2012) (Figures 1C–1F and 1J–1M), to produce the anatomically defined area boundaries which were used to assign electrodes to areas (Figures 1G and 1N). For the frequency bands analyzed here, ECoG signals reflect neuronal activity from both superficial and deep cortical layers (Watanabe et al., 2012). For the analysis of interareal synchronization and influences, we removed the common recording reference by subtracting signals from immediately neighboring electrodes from each other, to arrive at local bipolar derivations, which we will refer to as "sites" (see Experimental Procedures for details).

Interareal Synchronization Occurs in Narrow Theta, Beta, and Gamma Frequency Bands

Between pairs of sites from different areas, interareal synchronization is quantified by the coherence metric (see Experimental Procedures). For an example pair of areas, V1 and DP, the interareal coherence during visual stimulation and attention task performance ("postcue" period, see Figure 2), revealed three distinct and relatively narrow bands: a theta-, a beta-, and a gamma-frequency band (Figure 3A). This spectral pattern was consistent across interareal site pairs in both monkeys (Figures 3C and 3D), including areas V1 and V2 (see Figure S1 available online). We determined frequency-specific directed influences by calculating Granger-causal (GC) influences between all possible interareal pairs of sites (Dhamala et al., 2008). The spectrum of GC influences of site 1 onto site 2 quantifies, per frequency, the variance in site 2 that is not explained by the past of site 2, but by the past of site 1. For our example pair of areas, the V1-to-DP influence is a feedforward influence and the DP-to-V1 influence a feedback influence (Markov et al., 2014b). The GC

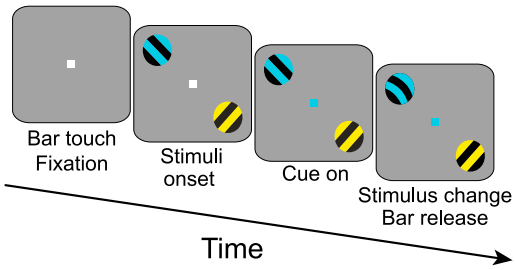

Figure 2. Selective Visual Attention Task

After touching a bar, the acquisition of fixation, and a prestimulus baseline interval of 0.8 s, two isoluminant and iso-eccentric stimuli were presented. In each trial, the light grating stripes of one stimulus were slightly tinted yellow and the stripes of the other stimulus were slightly tinted blue, assigned randomly. After a variable amount of time (1–1.5 s in monkey 1, 0.8–1.3 s in monkey 2), the color of the fixation point changed to blue or yellow, indicating the stimulus with the corresponding color to be the behaviorally relevant one. The "prestimulus" period was defined as the time period from fixation to stimulus onset, the "precue" period as the time from stimuli onset until cue presentation, and the "postcue" period as the time period from 0.3 s after cue onset until the first shape change in one of the stimuli. See Experimental Procedures for details.

feedforward influence was stronger than the feedback influence in the theta and gamma-bands, whereas the feedback influence was stronger in the beta-band (Figure 3B).

Asymmetries in Granger-Causal Influences Relate to Anatomical Asymmetries

To test whether this pattern held generally, we related GC influences to anatomical projections, specifically to a metric of their feedforward or feedback character. When retrograde tracer is injected into a target area, target-projecting neurons are labeled in all source areas. If a source area is providing feedforward input to the target area, the SLN of this projection, i.e., the proportion of [supragranular *l*abeled *n*eurons] relative to [supragranular plus infragranular labeled neurons] is high (Markov et al., 2014b). Vice versa, if a source area provides feedback input to the target, the SLN of this projection is low. Hence, the SLN metric quantifies the degree to which an interareal anatomical projection is feedforward or feedback (Figure 4A). We related SLN, across all interareal projections, to the corresponding GC influences (GCIs). We defined

$$[\mathrm{GCI}(\text{source->target}) - \mathrm{GCI}(\text{target->source})]/$$
$$[\mathrm{GCI}(\text{source->target}) + \mathrm{GCI}(\text{target->source})]$$

as the *d*irected influence *a*symmetry *i*ndex, or DAI. We correlated the DAI with the corresponding SLN values, across all area pairs (Spearman rank correlation between DAI values from two monkeys with ECoG recordings and SLN values from an independent set of 25 monkeys). Because the DAI is defined per frequency, the DAI-SLN correlation was also determined per frequency, and the resulting correlation spectrum is shown in Figure 4B. A positive DAI-SLN correlation for a given frequency indicates that this frequency channel conveys feedforward influences, and a negative correlation indicates feedback influences. Thus, the correlation spectrum demonstrates that feedforward influences are conveyed through theta- and gamma-frequency channels, and feedback influences are conveyed through a beta-frequency channel. Figure S2 shows the DAI-SLN correlation spectrum up to 250 Hz, demonstrating that GC influences in the broadband high-frequency range beyond the gamma-band are not systematically related to anatomical asymmetries. Figure S2 also shows that the DAI-SLN correlation spectrum was similar before the attentional cue was presented (precue period) and even before stimulus onset (prestimulus period).

Asymmetries in Granger-Causal Influences Define a Functional Hierarchy

The pattern of anatomical feedforward and feedback projections across all pairs of visual areas is largely consistent with a global hierarchy in which each area occupies a hierarchical level. This defines a given interareal projection as either bottom-up or top-down. Importantly, such a hierarchy is a global model fitted to all interareal projections, and the bottom-up (top-down) relationships derived from the global hierarchy agree only partly with the feedforward (feedback) characteristic found for individual interareal projections. The correlations between the anatomical SLN metric and the functional DAI metric suggest that it might be possible to construct a hierarchy of visual cortical areas from DAI values alone. This would demonstrate that not only the anatomical but also the functional relations across many pairs of areas are consistent with a global hierarchy. To explore this, we first used the postcue period and combined all evidence available in the DAIs across the frequency spectrum, by averaging the DAIs of the theta-, beta-, and gamma-frequency bands, after inverting the sign of the beta-band DAI, because of its negative correlation to SLN. This multifrequency band DAI (mDAI) was strongly correlated with the SLN across all pairs of areas (Figure 4C) ($R = 0.6$, $p < 1E^{-8}$, using Spearman rank correlation here and in the following correlation tests).

We proceeded to test whether a functional hierarchy could be derived from the mDAI values. First, the mDAI values, which can range from −1 to 1, were rescaled into a range from −5 to 5. This corresponds to the notion that there might be up to 10 distinct hierarchical levels (Felleman and Van Essen, 1991). Second, we considered each area in turn as target area, and shifted the rescaled mDAI values of all source areas such that the smallest value was one. This corresponds to the notion that, while interareal influences can be feedforward or feedback directed, resulting in positive or negative mDAI values, the resulting hierarchical levels are all positive, and the lowest hierarchical level is level one. Third, we averaged the resulting functional-hierarchical levels across all target areas and across the two monkeys. If the functional-hierarchical levels estimated for a given source area are consistent across target areas and animals, this will result in a small standard error, indicating that functional-hierarchical levels are well defined. If functional-hierarchical levels are well defined and furthermore differ between areas, this demonstrates that area-pairwise GC influences are largely consistent with a global hierarchy. Figure 4D (black dots) shows for the eight areas the resulting functional-hierarchical levels and their standard errors, demonstrating the existence of a GC-influence-based functional hierarchy. In Figure 4D, the different areas are ordered on the x axis according to increasing functional hierarchical level. This functional hierarchy correlates strongly with

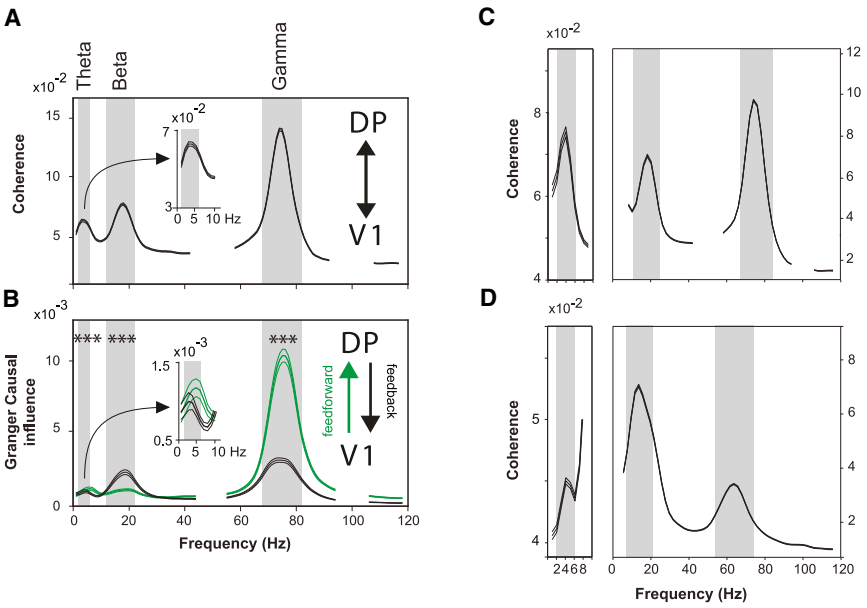

Figure 3. Example Coherence and Granger Causality Spectra and Average Coherence Spectra per Monkey

(A and B) (A) Coherence and (B) GC influence spectra for an example pair of areas: V1 and DP. Values in the ranges 45–55 Hz and 95–105 Hz are masked because of residual line noise. The example stems from monkey 1.

(C) For monkey 1, all interareal coherence spectra were averaged, and peaks were found using an automatic peak-detecting algorithm (see Experimental Procedures for details). To assess the theta peak with 1 Hz spectral resolution, the analysis of the lower frequencies used 1 s epochs and Hann tapering. The resulting band definitions are indicated by gray bars.

(D) Same as (C), but for monkey 2 (line noise masking not necessary).

the most recent anatomical hierarchy (Markov et al., 2014b) of visual cortex (R = 0.93, p = 0.002).

To probe the robustness of the functional hierarchy, one or multiple areas were removed and the functional hierarchy constructed on the remaining areas. The red dots in Figure 4D show that removal of V1 leaves the hierarchical positions of the remaining seven areas essentially unchanged. These positions were plotted against the positions from the full model as red dots in Figure 4E, demonstrating a strong correlation (R = 0.96, p = 0.003). This correlation remained significant even after removal of up to three areas from the lower end of the hierarchy, or up to two areas from the upper end (Figure 4E, other colors).

Functional Hierarchy Changes Dynamically with Behavioral Context

The functional hierarchy is defined by GC influences, with the intriguing consequence that it might change dynamically. This would require dynamic changes in GC influences between areas, which have been described, e.g., between FEF and V4 during the course of task performance (Gregoriou et al., 2009). Therefore, we investigated whether the functional hierarchy changed across different task periods. We found that the postcue hierarchy (shown again in Figure 5A) is already largely present during the precue period (Figure 5B). Areas V1, V2, V4, TEO, DP, and 7A arranged in their well-established order. However, 8L, the lateral part of FEF, assumes a lower level in the precue period (Figure 5B). In the prestimulus period (Figure 5C), both 8L and 8M move to the bottom of the hierarchy. Furthermore, V1, V2, and V4 move closer together. These analyses demonstrate that the DAI-based functional hierarchy is not fixed as are anatomy-based hierarchies. The most recent anatomy-based hierarchy (Markov et al., 2014b) shows an R = 0.93 correlation to the postcue functional hierarchy (Figure 5A, p = 0.002), an R = 0.91 correlation to the precue functional hierarchy (Figure 5B, p = 0.005), and no significant correlation to the prestimulus functional hierarchy (Figure 5C, p = 0.2). Once the stimulus and cue are present, interareal influences are most likely exerted in both bottom-up and top-down directions. Note that anatomical connections in the two directions are present at all times. This might explain why the anatomical hierarchy correlates particularly well with the functional hierarchy during the postcue period.

Global Consistency of the Functional and Anatomical Hierarchies

As mentioned above, the anatomical hierarchy is a global model fitted to all interareal projections, and the bottom-up (top-down) relationships derived from the global hierarchy agree only partly with the feedforward (feedback) characteristic found for individual interareal projections. Across the interareal anatomical projections considered here, 80% have a feedforward (feedback) characteristic that matches the relative position of the areas in the anatomical hierarchy (36/45 interareal projections with at least ten labeled neurons, see Experimental Procedures for details; defining feedforward as SLN > 0.5). Interestingly, across the interareal GC influences considered here, 86% have a feedforward (feedback) characteristic that matches the relative position of the areas in the functional hierarchy (24/28 area pairs; defining feedforward as mDAI > 0 during the postcue period). Thus, the degree of hierarchical organization appears similar in anatomy and function (p = 0.79, jackknife test across areas).

Individual interareal functional relationships also agreed in most cases with the anatomical hierarchy (Figures S3–S5). When separate tests (Bonferroni corrected across all tests) were performed per area pair, frequency band, and monkey, significant differences between GC influences in the two directions agreed with the anatomical hierarchy in 77% of cases (47 of 61, $p < 0.001$ across all tests; $p < 0.02$ for theta, $p < 0.03$ for beta, $p < 0.005$ for gamma; binomial tests).

Correspondingly, when we averaged GC influence spectra separately for the bottom-up and top-down directions, they showed clear differences. To determine which direction is bottom-up and which one top-down, we used the most recent

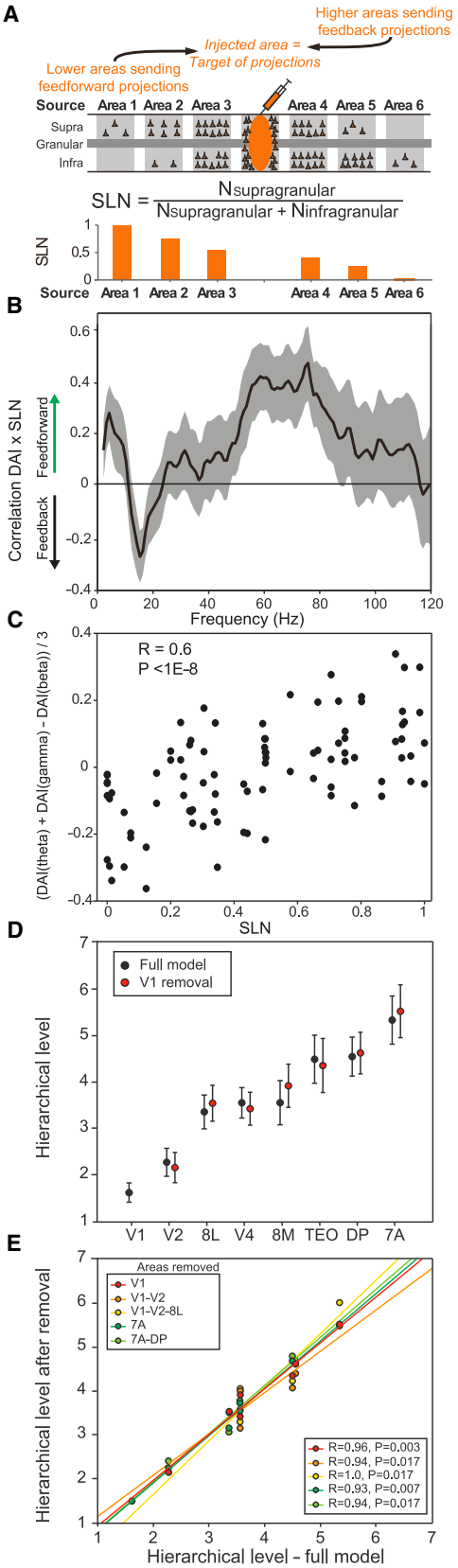

Figure 4. Granger-Causal Influences Correlate Directly with Anatomy and Establish a Functional Hierarchy

(A) Schematic of retrograde anatomical tracing method and calculation of SLN values. Retrograde tracer is injected into a target area and labels neurons in several source areas projecting to the target area. Source areas hierarchically lower (higher) than the target area have a progressively higher (lower) proportion of labeled neurons in the supragranular layers, i.e., the lower (higher) the source area relative to the target area, the higher (lower) the SLN value of the source-to-target projection.

(B) Spearman rank correlation across area pairs, between DAI values from two monkeys with ECoG recordings and SLN values from an independent set of 25 monkeys. This DAI-SLN correlation was calculated per frequency bin of the DAI, resulting in the spectrum. The gray-shaded region shows the 99.9% confidence interval, corresponding to a 95% confidence interval after correcting for the multiple comparisons across frequencies. Theta and gamma influences were related to anatomical feedforward projections, and beta influences to feedback projections. To assess the theta peak with 1 Hz spectral resolution, the analysis used 1 s epochs and Hann tapering. Only SLN values based on at least ten labeled neurons were included.

(C) Correlation between SLN and the DAI combined across theta-, beta-, and gamma-bands as specified on the y axis.

(D) Black dots indicate hierarchical levels for all areas, derived by taking each area in turn as target and assigning the hierarchical level to the other areas based on their GC influences to the target. Error bars show the SEM across target areas. Red dots indicate hierarchical levels after removing V1, revealing immunity to this manipulation.

(E) Red dots indicate hierarchical levels of the full model versus one with V1 removed. Other colors indicate corresponding analyses after removing more areas from the lower or upper end of the hierarchy.

anatomical hierarchy (Figure 6A) (Markov et al., 2014b) rather than the functional hierarchy, thereby avoiding circularity. We defined each area in turn as the target area, and averaged its GC influences to all other areas, separately for the bottom-up and top-down directions (Figure 6B). Theta-band influences were more bottom-up directed for seven of eight target areas (and not significantly different for the remaining area), beta-band influences were more top-down directed for all target areas, and gamma-band influences were more bottom-up directed for all target areas. In the grand average across all 28 pairs of areas and both animals, this pattern was highly significant (Figure 6C, $p = 0$ for each of the three frequency bands). The same held also for each monkey individually without alignment of frequency bands between animals (Figure 7, $p = 0$ for each of the three frequency bands and each animal).

Additional analyses showed that this pattern was not due to observation noise (Nalatore et al., 2007) (Figures S6A and S6B) or the bipolar derivation scheme (Figures S6C and S6D). Regarding the theta-band, we note that the visual cortical theta rhythm is partly locked to microsaccades (Bosman et al., 2009). Therefore, theta-rhythmic microsaccades with corresponding retinal image motion and subsequent visual responses might contribute to the feedforward GC influences in the theta-band. For the gamma-band, an analysis that excluded microsaccade effects left the pattern of GC influences unchanged (Figures S6E and S6F). We also performed a conditional GC influence analysis (Wen et al., 2013), which aimed at estimating the GC influences that two areas exert directly onto each other, while excluding influences mediated by any one of the remaining visual areas. This analysis left the pattern of results unchanged for gamma and beta, and suggested the involvement of larger networks for theta (Figure S7).

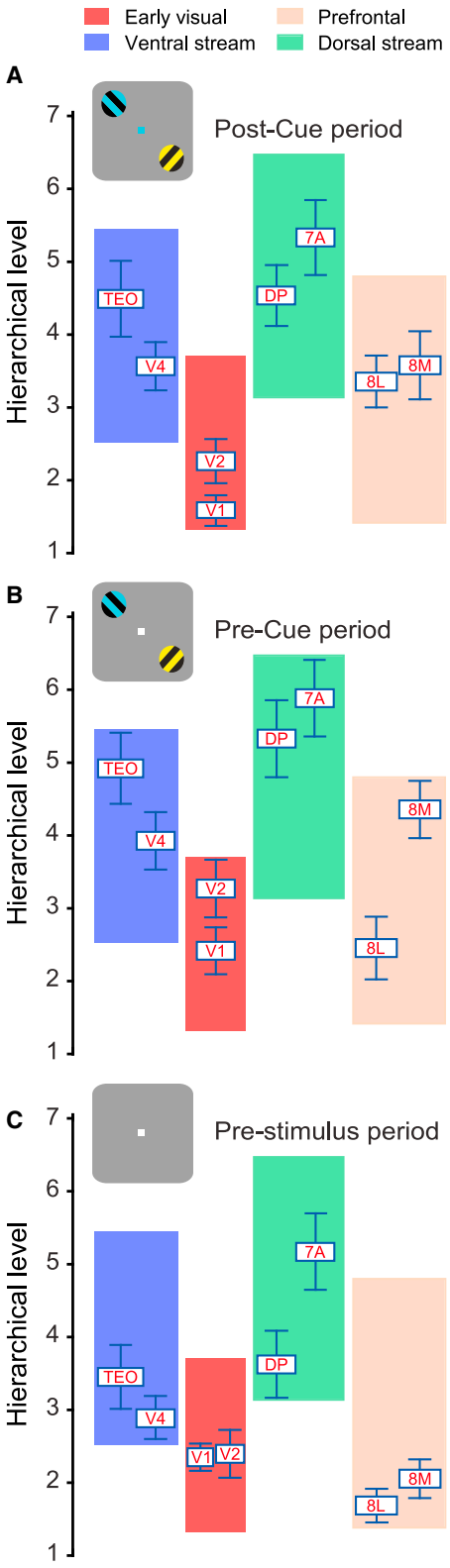

Figure 5. The Functional Hierarchy Is Dynamic

The dynamics of the functional hierarchy with cognitive context is shown through three main periods of the task.

(A) The postcue period, when the stimulus was on, the attentional cue had been given and attention had been deployed.

(B) The precue period, when the stimulus was on, but the attentional cue had not yet been given.

(C) The prestimulus period, when the animal was fixating, but the stimulus was not yet presented. Each area's mean hierarchical position is depicted relative to the others. Error bars indicate standard error of the mean in the hierarchical position across the different areas taken as targets.

Attention Enhances Top-Down and Bottom-up Influences in a Spatially Specific Manner

Finally, we tested the prediction that top-down beta-band influences are enhanced when a cognitive task requires stronger top-down control. Top-down control is expected to be enhanced by selective attention. Indeed, when selective attention was directed to the contralateral as compared to the ipsilateral stimulus, top-down beta-band GC influences were enhanced in the grand average ($p < 0.001$) and in all pairs of areas with a significant attention effect ($n = 13$, $p < 0.0005$, binomial test). This enhanced top-down beta-band influence might lead to enhanced bottom-up gamma-band influences (Bressler and Richter, 2014; Lee et al., 2013). Indeed, when selective attention was directed to the contralateral as compared to the ipsilateral stimulus, bottom-up gamma-band GC influences were enhanced in the grand average ($p < 0.001$) and in 93% of area pairs with a significant attention effect ($n = 13/14$, $p < 0.002$, binomial test).

DISCUSSION

In summary, we have shown that among primate visual cortical areas, feedforward communication utilizes the theta and gamma-bands and feedback communication the beta-band. As gamma-band synchronization predominates in superficial and beta-band synchronization in deep cortical layers (Buffalo et al., 2011; Roberts et al., 2013; Xing et al., 2012), these asymmetries in directed influences are likely related to the laminar pattern of interareal anatomical projections. Future studies might test this directly with simultaneous multiarea multilayer recordings of LFP and spikes, and extend coverage to more cortical and subcortical structures, and the previous laminar analyses (Buffalo et al., 2011; Roberts et al., 2013; Xing et al., 2012) to the theta-band.

Feedforward and feedback interareal influences need to fulfill different requirements, which might be met by synchronization in different frequency bands. It is conceivable that interareal synchronization entails higher energetic costs for gamma than beta (Niessing et al., 2005), and bottom-up signaling might be equipped with the gamma-band rhythm in order to achieve higher communication throughput. Inputs may have differential effects at their target structure uniquely due to the rhythm through which they have been transferred. For example, target cells and/or local circuits with resonant properties in particular frequency bands might be addressed differentially by inputs with different rhythms (Hasenstaub et al., 2005; Lee et al., 2013; Wang, 2010). In that sense, the frequency band through which an input is mediated might functionally tag that input for differential further processing.

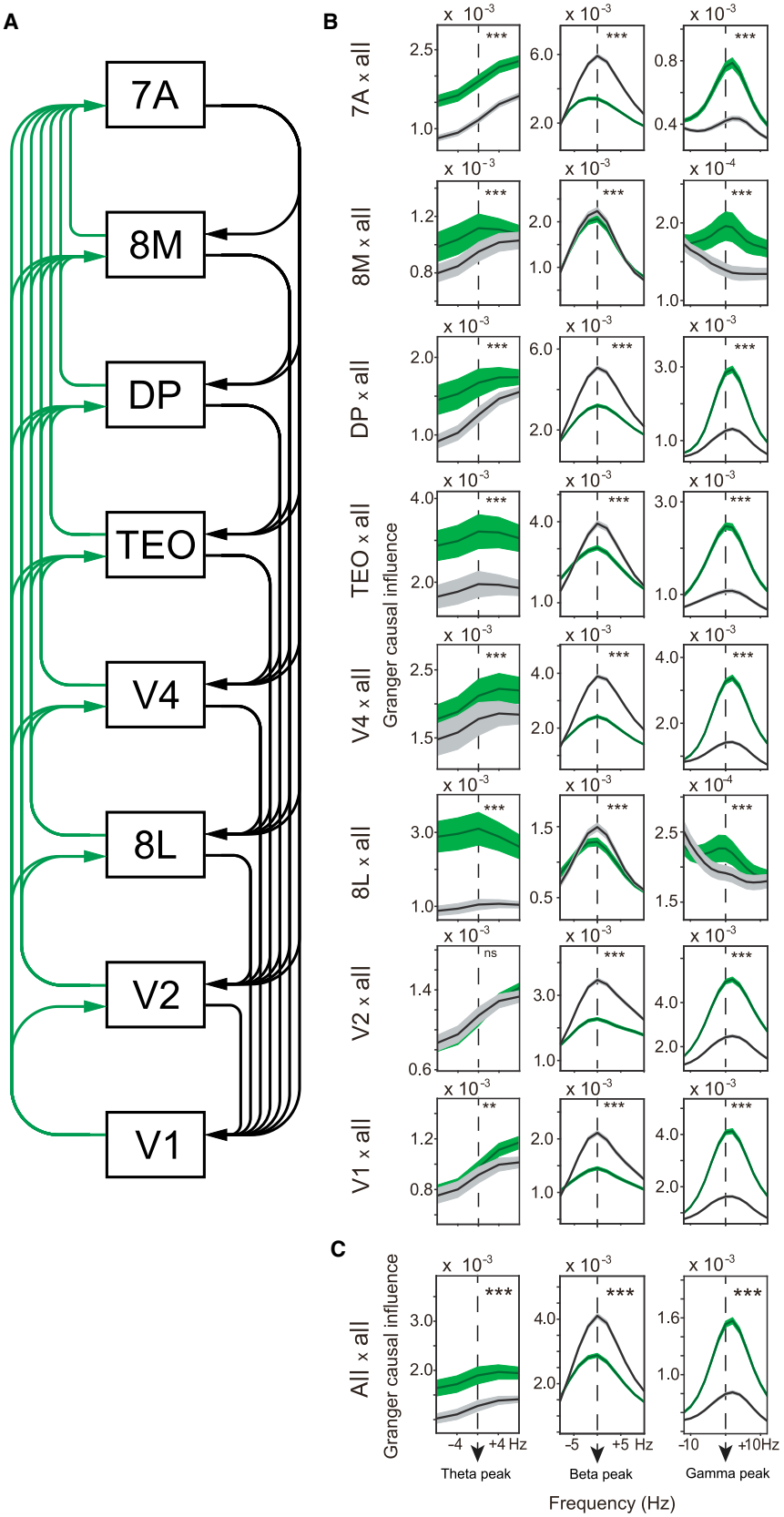

Figure 6. Granger-Causal Influences in the Bottom-Up and Top-Down Directions

(A) Hierarchical ranking of the recorded visual areas according to the most recent anatomical hierarchical model (Markov et al., 2014b). This hierarchical model specifies each interareal influence as either bottom-up (green arrows) or top-down (black arrows).

(B) For each row, the area indicated on the left was taken as target area. The target area's GC influences to all other areas were sorted into bottom-up and top-down influences as indicated by the green and black arrows in (A). Average bottom-up spectra are shown in green, average top-down spectra in black. Spectra were averaged across monkeys after aligning frequency peaks.

(C) Same as (B), but grand averaging across all target areas.

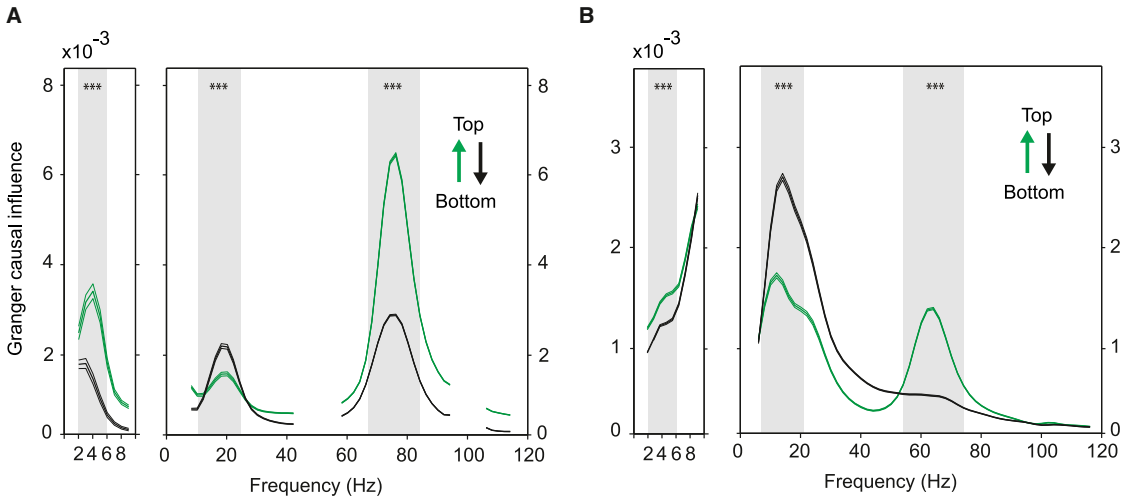

Figure 7. Granger-Causal Influence Spectra in the Bottom-Up and Top-Down Directions per Monkey

(A) GC influence spectra averaged over all interareal site pairs, separately for the bottom-up and top-down direction (as indicated by the color legend) in monkey 1. Hierarchical position of each area was determined based on the most recent anatomical hierarchical model of the visual system (Markov et al., 2014b). GC influence values in the range from 45–55 Hz and 95–105 Hz are masked because of residual line noise. To assess the theta peak with 1 Hz spectral resolution, the analysis of the lower frequencies used 1 s epochs and Hann tapering.

(B) Same as (A), but for monkey 2 (line noise masking not necessary). ***$p < 0.001$.

We have demonstrated that functional hierarchy exhibits dynamic changes. This might be due to differential activation of superficial and deep layers. Specific activation of the superficial layers of a source area could increase its gamma-band influence on target areas. This increased gamma-band influence will move the source area to a lower level of the hierarchy. By contrast, if the deep layers of an area are activated, this might enhance its beta-band influence on other areas, thereby moving the area up the hierarchy. Future multilayer recordings in multiple areas can test these predictions. These recordings would be particularly useful during cognitive tasks that systematically manipulate the amount of feedforward and feedback signaling.

Such tasks might be derived from the conceptual framework of predictive coding (Bastos et al., 2012). This framework holds that statistical regularities of sensory inputs are learned by shaping feedforward connectivity and thereby response properties of higher-area visual neurons, and that these neurons in turn continuously feedback predictions to lower areas. Lower areas then feed forward only the difference between the prediction and the actual input, i.e., the prediction error. When prediction errors again reach higher areas, they influence predictions in an accumulative fashion. This accumulation constitutes a low-pass filter such that predictions change slower than prediction errors (Friston, 2008). The more rapidly changing prediction errors might require the gamma rhythm for being fed forward. At the same time, the low-pass filtering entailed in generating predictions might render the beta rhythm ideal for feedback. The segregation of feedforward and feedback processing through distinct frequencies and layers has been proposed as a key architectural feature of circuits involved in predictive coding (Bastos et al., 2012).

Indeed, several previous studies have found that conditions entailing the feedback of predictions led to increased oscillations in relatively lower frequencies, and conditions entailing the feeding forward of prediction errors led to increased oscillations in relatively higher frequencies. For example, a study in the cat visual system investigated rhythmic synchronization between primary visual cortex (area 17) and visual association cortex (area 7), while cats observed either expected or unexpected visual stimuli (von Stein et al., 2000). When expected stimuli matched the prediction and triggered a go response, synchronization was strongest in a 4–12 Hz band; when unexpected stimuli induced a prediction error, synchronization was strongest in the gamma-frequency band. A magnetoencephalography study in human subjects used audiovisual speech to generate conditions in which auditory speech signals either matched or violated predictions based on visual speech (Arnal et al., 2011). When visual speech correctly predicted auditory input, rhythmic brain responses were dominated by a 3–4 Hz response. By contrast, when auditory input violated vision-based predictions, this led to a response in a 14–15 Hz and a 60–80 Hz band. In both of these studies, the response to the predicted stimulus entailed a lower and the response to the unpredicted stimulus a higher frequency band. Similarly, a recent study in rodent hippocampus compared track runs with retrospective and prospective coding (Bieri et al., 2014). During retrospective coding, place fields reflect recently visited locations and therefore likely memory encoding. During prospective coding, place fields reflect upcoming locations and therefore likely memory retrieval. Runs with retrospective and prospective coding occur spontaneously intermingled. During retrospective coding, relatively faster gamma (60–100 Hz), and during prospectively coding, relatively slower gamma (25–55 Hz) occurs in hippocampus. We would like to tentatively identify retrospective coding and memory encoding with feedforward signaling of prediction errors during fast gamma, and prospective coding and memory retrieval with feedback signaling of

predictions during slow gamma (Fries, 2009). A similar rationale might hold when prediction is not related to long- but to short-term memory. In one study, a cue stimulus was encoded into short-term memory, then disappeared for a delay period and subsequently had to be found in an array comprising the cue among three distracters (Buschman and Miller, 2007). In a search condition, distracters differed from each other and therefore, the cue had to be fed back from short-term memory stores for comparison with the array stimuli. In a pop-out condition, all distracters were identical and the task could be performed on feedforward signals alone. Compared to the pop-out task, the search task enhanced prefrontal-parietal coherence in a 22–34 Hz frequency band and reduced it in a 35–55 Hz frequency band. Thus again, the condition requiring feedback involved stronger synchrony in a lower frequency band, and the condition requiring the feeding forward of a salient sensory stimulus involved stronger synchrony in a higher frequency band.

As intriguing as these results are, the operationalization of feedforward versus feedback signaling through cognitive tasks remains a challenge. For example, a particularly clean way to operationalize top-down signaling is by means of selective visual attention. During a selective visual attention task, attention in different trials is placed onto one of several stimuli that are equal in terms of size, contrast and eccentricity, such that attending to either individual stimulus is expected to be equally difficult. Because sensory stimuli remain identical across attention conditions, bottom-up signaling also appears to be controlled. However, when attention is placed onto a stimulus and enhanced top-down signals reach the visual cortical representation of the attended stimulus, this is expected to cause enhanced bottom-up signaling of that stimulus (Lee et al., 2013). In agreement with this expectation, bottom-up GC influences from V1 to V4 are enhanced when they signal the attended stimulus (Bosman et al., 2012). Thus, enhanced bottom-up signaling can be a consequence of enhanced top-down signaling, and even a selective attention paradigm, that is controlled for difficulty and sensory stimulation, does not disentangle the two by means of a simple cognitive contrast. Therefore, we based our present analysis not on a comparison between cognitive conditions, but rather on a comparison of GC influences with the feedforward or feedback character of the corresponding anatomical projections.

Finally, we note that the definition of the functional hierarchy through the assessment of interareal GC influences might be transferrable to human experiments. In human subjects, post-mortem interareal tracer studies have so far met strong technical limitations. By contrast, intracranial LFP recordings (Tallon-Baudry et al., 2001) and/or MEG recordings together with source analysis (Siegel et al., 2008) might offer an opportunity to arrive at a hierarchical model of the human brain, including uniquely human brain areas, by capitalizing on the functional hierarchy presented here.

EXPERIMENTAL PROCEDURES

Summary

Two adult male rhesus monkeys performed a visual attention task, during which they fixated a central spot and released a bar when the behaviorally relevant stimulus underwent a shape change (Figure 2). Behavioral relevance was assigned on a trial-by-trial basis with a centrally presented cue. Two stimuli were presented, one in the lower right visual hemifield and one in the upper left visual hemifield. Neuronal signals were recorded from the left hemisphere in two monkeys using subdural ECoG grids consisting of 252 electrodes (1 mm diameter), which were spaced 2–3 mm apart (Bosman et al., 2012; Brunet et al., 2013, 2014; Rubehn et al., 2009). Data were recorded in 9 sessions in monkey 1 and 14 sessions in monkey 2. The postcue analysis used the time period from 0.3 s after cue onset until the first shape change in one of the stimuli. Only trials with a correct behavioral report were used. For each trial, this period was cut into nonoverlapping 0.5 s data epochs. This resulted in 3,874 epochs for monkey 1 and 3,492 epochs for monkey 2. For both the prestimulus and precue periods, there were 4,239 and 4,396 epochs of 0.5 s in monkey 1 and 2, respectively. For each site and recording session, the data epochs were normalized by their standard deviation and subsequently pooled across sessions. Data epochs were multitapered using three Slepian tapers and Fourier-transformed (Mitra and Pesaran, 1999). The epoch lengths of 0.5 s resulted in a spectral resolution of 2 Hz and the multitapering in a spectral smoothing of ±3 Hz. Where mentioned explicitly, we used Hann-tapered 1 s epochs for 1 Hz spectral resolution. The Fourier transforms were the basis for calculating the coherence spectra and for calculating the GC influence spectra through nonparametric spectral matrix factorization (Dhamala et al., 2008). The nonparametric estimation of GC influences spectra has certain advantages over parametric approaches, e.g., it does not require the specification of a particular autoregressive model order.

Experimental Paradigm

All procedures for the electrophysiological recordings were approved by the ethics committee of the Radboud University Nijmegen (Nijmegen, The Netherlands). After touching a bar, the acquisition of fixation, and a prestimulus baseline interval of 0.8 s, two isoluminant and isoeccentric stimuli (drifting sinusoidal gratings, diameter: 3 degrees, spatial frequency: ~1 cycles/degree, drift velocity: ~1 deg/s, resulting temporal frequency: ~1 cycle/s, contrast: 100%) were presented on a CRT monitor (120 Hz refresh rate noninterlaced). In each trial, the light grating stripes of one stimulus were slightly tinted yellow, and the stripes of the other stimulus were slightly tinted blue, assigned randomly (Figure 2). After a variable amount of time (1–1.5 s in monkey 1, 0.8–1.3 s in monkey 2), the color of the fixation point changed to blue or yellow, indicating the stimulus with the corresponding color to be the behaviorally relevant one. A trial was considered correct and the monkey was rewarded when the bar was released within 0.15–0.5 s of the change in the cued stimulus. No reward but a timeout was given when monkeys released the bar in response to equally likely changes of the noncued stimulus. In monkeys 1 and 2, 94% and 84% of bar releases, respectively, were correct reports of changes in the relevant stimulus. The stimulus change consisted of the stimulus' stripes undergoing a gentle bend, lasting 0.15 s. Either one of the stimuli, irrespective of being cued or not, could change at a random time between stimulus onset and 4.5 s after cue onset. Trials were terminated without reward when the monkey released the bar outside the response window, or when it broke fixation (fixation window, 0.85 degree radius in monkey 1, 1 degree radius in monkey 2). For the analyses presented here, if not specified otherwise, data from all correct trials of both attention conditions were pooled.

Neurophysiological Recordings

The ECoG grids were implanted under aseptic conditions with isoflurane/fentanyl anesthesia. Intraoperative photographs were acquired for later coregistration (Figures 1A and 1H). Signals were amplified, high-pass filtered at 0.159 Hz, low-pass filtered at 8 kHz, and digitized at roughly 32 kHz with a Neuralynx Digital Lynx acquisition system. Local Field Potentials were obtained by low-pass filtering at 250 Hz and down sampling to 1 kHz.

Electrodes were recorded through eight 32-channel headstages, against a silver wire implanted epidurally over right occipital cortex, which served as common recording reference. Offline, the signals were re-referenced to remove the common recording reference and thereby preclude it from affecting coherence and GC influence. For re-referencing, we chose the bipolar derivation scheme as explained in detail below. Each bipolar derivation removed the common recording reference while using only two electrodes with a constant interelectrode distance and taken from the same finger and the same lane of

the ECoG grid. The electrodes were arranged in lanes (Figures 1B and 1I). Two neighboring lanes always ran parallel on one "finger" of the polyimide foil that provided the backbone of the array (Rubehn et al., 2009). The lanes ran mediolaterally over most of the covered region and posterioanteriorally at the frontal end of the covered region. In Figure 1, electrodes recorded through the same headstage are shown in the same color, and electrodes on alternating lanes in dark/light, such that electrodes of the same lane and recorded through the same headstage were given the same color and darkness. If not stated otherwise, all analyses used bipolar derivations, i.e., sample-by-sample differences between immediately neighboring electrodes. Bipolar derivations were obtained for all pairs of immediately neighboring electrodes on the same lane, which were also recorded through the same headstage. As mentioned above, this realized several aims: (1) Bipolar derivation cleanly removed the common recording reference. (2) Each bipolar derivation used only two immediately neighboring electrodes and thereby minimal space, which allowed optimal attribution of the resulting signals to cortical areas. Bipolar derivations were only used when both electrodes had been assigned to one and the same area, whereas pairs of electrodes that crossed area boundaries were discarded. (3) The use of two electrodes that neighbored each other along a lane of a given finger ensured a constant distance of 2.5 mm along the cortical surface. (4) The use of electrode pairs from the same lane almost always allowed using electrodes amplified by the same headstage. The few bipolar derivations that bridged from one headstage to the next were discarded. Each headstage introduced headstage-specific noise into all signals amplified through that headstage, probably by the headstage-wise reference amplification. Bipolar derivation using electrode pairs recorded through the same headstage removed headstage-specific noise, whereas bipolar derivation using electrode pairs recorded through two separate headstages would have summed the headstage-specific noises. For these reasons, the particular rereferencing scheme was optimal for the purposes of this study. Other studies might benefit from different referencing schemes, e.g., if the absolute phase of a rhythm needs to be assessed. While the absolute phase is irrelevant for both the coherence and the GC influence metric, and therefore the direction of differentiation does not change the results, we document that for the mediolaterally running lanes, the bipolar derivation was calculated as [(lateral electrode) − (medial electrode)], and for the posterior-anteriorly running lanes, the bipolar derivation was calculated as [(anterior electrode) − (posterior electrode)].

As an explicit control for the arbitrary absolute phases obtained from bipolar derivations, we also used a current-source density (CSD) approach (Figures S6C and S6D). For each CSD site, three immediately neighboring electrodes along a lane of electrodes and recorded through the same headstage were used, and the average signal of the two flanking electrodes was subtracted from the signal of the central electrode. CSDs were assigned to the area in which the central electrode was located. If neighboring areas shared an electrode in one of their CSDs, this CSD was excluded from the area with the larger number of electrodes when calculating coherence or GC influences between those areas.

Data Analysis General

Data analysis used the FieldTrip toolbox (Oostenveld et al., 2011). Power line artifacts at 50, 100, and 150 Hz were estimated and subtracted from the data using a Discrete Fourier Transform. We defined individual beta and gamma-bands in each monkey by using a peak detection algorithm that searched blindly across the coherence spectrum averaged across all site pairs of all visual areas (Figures 3C and 3D). The algorithm fitted parabolas to the peaks. Frequency bands were defined by the resulting peak frequencies and the full width at half maximum. For the postcue period, this resulted in the following bands: in monkey 1, the gamma-band was 67–83 Hz (peak frequency was 74Hz), and the beta-band was 12–24 Hz (peak frequency was 18 Hz). In monkey 2 the gamma-band was 54–74 Hz (peak frequency was 64 Hz), and the beta-band was 7–21 Hz (peak frequency was 14 Hz). The theta-band was defined on individual peaks of the coherence spectrum averaged across all site pairs of all visual areas and taking half of the maximum as width. This resulted in the following theta-band for both monkeys: 2–6 Hz (peak frequency was 4 Hz). In both monkeys, the gamma, beta, and theta-band peaks were the only peaks detected in these average spectra. The same method was applied for the definition of individual beta- and gamma-bands in the other periods of the task, the prestimulus period from fixation to stimulus onset, and the precue period from stimulus onset until cue presentation (Figure 2). This gave nearly identical results, except for the period preceding stimulus onset, where no gamma peak could be detected in the average spectra and correspondingly, the gamma-band was not included in Figures 5C and S5.

Analysis of Conditional Granger-Causal Influences

For the computation of conditional GC influences, we used multivariate nonparametric spectral matrix factorization (mNPSF). The input to the mNPSF algorithm consists of the complete cross-spectral density matrix. In the original data, the number of power and crossspectra was 4,753 in monkey 1 (97 sites) and 5,886 in monkey 2 (108 sites). For the mNPSF algorithm to converge, the input size had to be reduced. Therefore, the bipolar derived signals were low-pass filtered with a cutoff at 90 Hz and downsampled to 300 Hz. Subsequently, a principal component analysis (PCA) on the time courses of all signals from a given area was performed, and only the principal components (PCs) that explained most variance were kept, until at least 90% of the variance of that area was explained. This reduced the number of power and cross spectra to 2,701 in monkey 1 (73 PCs) and to 3,240 in monkey 2 (80 PCs). Thus, input to the mNPSF algorithm was reduced by 43% in monkey 1 and 45% in monkey 2.

The analysis of regular, i.e., nonconditional, GC influences gave similar results when applied to the original data and after those reduction steps, i.e., there was a strong correlation between DAIs (see main text for definition) with and without reduction (theta, $R = 0.82$, $p = 2E^{-14}$; beta, $R = 0.88$, $p = 3E^{-19}$; gamma, 0.74, $p = 1E^{-10}$). Therefore, regular GC influence analyses did not use these reduction steps.

We computed blockwise, conditional GC influences between each pair of areas, treating the PCs representing all other areas as the block to be conditioned on (Wen et al., 2013). Consider the PCs belonging to area 1, to area 2, and to the remaining areas. To compute the conditional GC influence that area 1 exerts onto area 2, conditioned on the rest, we performed mNPSF on two cross-spectral density matrices: (1) on the cross-spectral density matrix containing all PCs, and (2) on the cross-spectral density matrix containing PCs from area 2 and the remaining areas to be conditioned on. The resulting transfer functions and noise covariance matrices from the two factorizations are used to derive the GC influence from area 1 onto area 2, conditioned on the rest, which quantifies, per frequency, the unique variance in area 1 that contributes to predictions about area 2, above and beyond the variance present in the other areas. This procedure was repeated for all possible pairs of areas, in both directions.

Analysis Excluding Microsaccade Effects for the Gamma-Band

Horizontal and vertical eye position was monitored at 230 Hz. Microsaccades (MSs) were detected using a velocity threshold of 5 SD. We selected all pairs of MSs that were separated by at least 0.8 s. Of those 0.8 s, we discarded 0.3 s post-MS and used the remaining 0.5 s for the analysis. At 0.3 s after a microsaccade, the LFP gamma phase is no longer locked to the microsaccade, and it is generally not phase-locked to an upcoming microsaccade (Bosman et al., 2009). Thus, these 0.5 s epochs were used to analyze GC influences in the absence of any effects from gamma locking to microsaccades.

Region of Interest Definition

For both monkeys implanted with ECoG grids, individual structural MRIs were acquired and the brains were segmented. ECoG electrode positions were co-registered with the segmented brains based on high-resolution intraoperative photographs, using the sulci for alignment (Figure 1). In order to assign an electrode to a cortical area, we co-registered the individual segmented brains to the F99 template brain (CARET v5.62). On the F99 brain, several different monkey brain atlases are defined (Felleman and Van Essen, 1991; Markov et al., 2011, 2014a; Paxinos et al., 1999): "Felleman and Van Essen.1991 (FVE91)," "Paxinos et al.2000 (PHT00)," "Markov et al.2010 (CC10)," and "Markov et al.2012 (CC12)." These atlases were projected onto the individual segmented brains (Figure 1). Thereby, for each atlas, each ECoG electrode was assigned to a cortical area. Across atlases, an electrode was assigned to the area to which it was assigned in the majority of atlases. If there was a tie, we considered a fifth atlas, not available in CARET, namely the atlas by Saleem and Logothetis (Saleem and Logothetis, 2007). With regard to 7A,

one of the atlases ("Paxinos et al.2000") distinguishes between the more lateral 7A/PG and the more medial 7A/OPT. The majority of 7A studies concerned with visual function have dealt with 7A/OPT (Constantinidis and Steinmetz, 2001a, 2001b; Raffi and Siegel, 2005; Rawley and Constantinidis, 2010), and also the 7A retrograde tracer injection used here, targeted the medial part of 7A (Markov et al., 2014a), i.e., was most consistent with an injection in 7A/OPT. Therefore, we restricted our definition of 7A to 7A/OPT and defined the lateral boundary of 7A according to "Paxinos 2000." After final electrode assignment, we selected the electrodes assigned to the areas V1, V2, V4, TEO, 8L, 8M, DP, and 7A (Figure 1). Bipolar derivations were used in the analysis only when both electrodes had been assigned to one and the same area, excluding pairs of electrodes that crossed area boundaries. The resulting sites (i.e., bipolar derivations) were distributed as follows: Monkey 1: V1: 31 sites, V2: 9 sites, V4: 19 sites, DP: 10 sites, TEO: 5 sites, 8/FEF: 15 sites (8M: 7 sites; 8L: 8 sites), 7A: 8 sites; Monkey 2: V1: 50 sites, V2: 14 sites, V4: 18 sites, DP: 8 sites, TEO: 3 sites, 8/FEF: 5 sites (8M: 2 sites; 8L: 3 sites), 7A: 10 sites.

Retrograde Tracer Database

Description of the anatomical data set acquisition and analysis has been reported in (Markov et al., 2014a). The values that we used correspond to multiple injections each into V1, V2, V4 and single injections into areas DP, TEO, 8/FEF (8L and 8M) and 7A. SLN values were obtained as described in Figure 4A (Markov et al., 2014b). For the correlation with DAI values, only SLN values based on at least 10 labeled neurons were included. Updates, atlases and additional information concerning the anatomical data set that was used for this work is available at www.core-nets.org.

Statistical Testing

We first tested for each area pair, whether the average GC influence between all interareal site pairs was significant, i.e., whether it reliably exceeded the bias level. We estimated the bias by randomly pairing epochs before GC influence calculation. For each of 500 randomizations, the mean over the GC influences in the two directions was placed into a randomization distribution and the 95th percentiles of the resulting distributions were used to determine the bias level. Every interareal GC influence reported in Figures S3, S4, and S5 exceeded the bias level.

For a given GC influence, we used the bootstrap method (100 bootstrap iterations) across epochs to estimate the 95% confidence intervals in order to determine whether the GC influences in the bottom-up and top-down directions were significantly asymmetric (Efron and Tibshirani, 1994). Confidence intervals and the resulting statistics are reported in Figures 3, 6, 7, and S3–S6. Under the null hypothesis, GC influences in the bottom-up and top-down directions stem from the same distribution and their expected difference is zero. Therefore, observed differences between bottom-up and top-down GC influences were tested against that value of zero. The bootstrap method was also used to estimate 95% confidence intervals for the coherence spectra in Figures 3, S1, and S3–S5.

In the analysis shown in Figures 4B and S2, we used the Spearman rank correlation and the bootstrap method across epochs to estimate the 99.9% confidence interval, corresponding to a 95% confidence interval after correcting for the multiple comparisons across frequencies.

All other reported correlation coefficients are also based on the Spearman rank correlation. This pertains to the following figures and/or the corresponding text: Figures 4C–4E, 5, S7C, and S7D.

To test whether attention modulated top-down beta-band influences and bottom-up gamma-band influences, we used a randomization approach. The null hypothesis is that influences during the two attention conditions stem from the same distribution. Therefore, under the null hypothesis, attention condition labels can be randomly assigned. For every epoch in the post-cue period, we randomly assigned the conditions "attention contralateral" and "attention ipsilateral." We computed GC influence for all area pairs at the monkey-specific frequency bands, and the difference between the conditions. This procedure was repeated 1,000 times, creating a randomization distribution that realized the null hypothesis. We then compared the empirically observed differences between GC influences during attention contralateral versus attention ipsilateral, to this randomization distribution. If the empirically observed difference was larger than the 97.5th percentile or smaller than the 2.5th percentile of the randomization distribution, the observed effect was deemed significant at $p \leq 0.05$.

SUPPLEMENTAL INFORMATION

Supplemental Information includes seven figures and can be found with this article at http://dx.doi.org/10.1016/j.neuron.2014.12.018.

AUTHOR CONTRIBUTIONS

C.A.B. and P.F. designed the experiments; C.A.B. trained the monkeys and recorded the electrophysiological data; P.F., P.D.W., and C.A.B. implanted the monkeys; J.-M.S., R.O., C.A.B., A.M.B., and J.V. wrote analysis programs; A.M.B., J.V., and J.-M.S. performed analyses with the help of R.O. and with the advice of P.F.; H.K. provided the anatomical data (SLN); J.R.D. contributed to the microsaccade analysis; A.M.B., J.V., and P.F. wrote the paper in collaboration with P.D.W, C.A.B., J.-M.S., and H.K.

ACKNOWLEDGMENTS

This work was supported by Human Frontier Science Program Organization Grant RGP0070/2003 (P.F.), Volkswagen Foundation Grant I/79876 (P.F.), the European Science Foundation European Young Investigator Award Program (P.F.), the European Union (HEALTH-F2-2008-200728 to P.F.), the LOEWE program ("Neuronale Koordination Forschungsschwerpunkt Frankfurt" to P.F.), the Smart Mix Programme of the Netherlands Ministry of Economic Affairs and the Netherlands Ministry of Education, Culture and Science (BrainGain to P.F., R.O., and J.-M.S.), The Netherlands Organization for Scientific Research Grant 452-03-344 (P.F.), the National Science Foundation Graduate Student Fellowship 2009090358 (A.M.B.), a Fulbright grant from the U.S. Department of State (A.M.B.), ANR-11-BSV4-501 (H.K.), and LabEx CORTEX (ANR-11-LABX-0042 to H.K.). The authors thank Matthew Nelson for helpful comments on an earlier version of this paper. A.M.B. would like to thank G.R. Mangun and W.M. Usrey for support.

Accepted: December 5, 2014
Published: December 31, 2014

REFERENCES

Arnal, L.H., Wyart, V., and Giraud, A.L. (2011). Transitions in neural oscillations reflect prediction errors generated in audiovisual speech. Nat. Neurosci. *14*, 797–801.

Bastos, A.M., Usrey, W.M., Adams, R.A., Mangun, G.R., Fries, P., and Friston, K.J. (2012). Canonical microcircuits for predictive coding. Neuron *76*, 695–711.

Bieri, K.W., Bobbitt, K.N., and Colgin, L.L. (2014). Slow and fast γ rhythms coordinate different spatial coding modes in hippocampal place cells. Neuron *82*, 670–681.

Bosman, C.A., Womelsdorf, T., Desimone, R., and Fries, P. (2009). A microsaccadic rhythm modulates gamma-band synchronization and behavior. J. Neurosci. *29*, 9471–9480.

Bosman, C.A., Schoffelen, J.M., Brunet, N., Oostenveld, R., Bastos, A.M., Womelsdorf, T., Rubehn, B., Stieglitz, T., De Weerd, P., and Fries, P. (2012). Attentional stimulus selection through selective synchronization between monkey visual areas. Neuron *75*, 875–888.

Bressler, S.L., and Richter, C.G. (2014). Interareal oscillatory synchronization in top-down neocortical processing. Curr. Opin. Neurobiol. *31C*, 62–66.

Brunet, N., Bosman, C.A., Roberts, M., Oostenveld, R., Womelsdorf, T., De Weerd, P., and Fries, P. (2013). Visual cortical gamma-band activity during free viewing of natural images. Cereb. Cortex. http://dx.doi.org/10.1093/cercor/bht280.

Brunet, N.M., Bosman, C.A., Vinck, M., Roberts, M., Oostenveld, R., Desimone, R., De Weerd, P., and Fries, P. (2014). Stimulus repetition modulates gamma-band synchronization in primate visual cortex. Proc. Natl. Acad. Sci. USA *111*, 3626–3631.

Buffalo, E.A., Fries, P., Landman, R., Buschman, T.J., and Desimone, R. (2011). Laminar differences in gamma and alpha coherence in the ventral stream. Proc. Natl. Acad. Sci. USA *108*, 11262–11267.

Buschman, T.J., and Miller, E.K. (2007). Top-down versus bottom-up control of attention in the prefrontal and posterior parietal cortices. Science *315*, 1860–1862.

Constantinidis, C., and Steinmetz, M.A. (2001a). Neuronal responses in area 7a to multiple-stimulus displays: I. neurons encode the location of the salient stimulus. Cereb. Cortex *11*, 581–591.

Constantinidis, C., and Steinmetz, M.A. (2001b). Neuronal responses in area 7a to multiple stimulus displays: II. responses are suppressed at the cued location. Cereb. Cortex *11*, 592–597.

Dehaene, S., Kerszberg, M., and Changeux, J.P. (1998). A neuronal model of a global workspace in effortful cognitive tasks. Proc. Natl. Acad. Sci. USA *95*, 14529–14534.

Dhamala, M., Rangarajan, G., and Ding, M. (2008). Estimating Granger causality from fourier and wavelet transforms of time series data. Phys. Rev. Lett. *100*, 018701.

Efron, B., and Tibshirani, R.J. (1994). An Introduction to the Bootstrap. (Boca Raton, Fla.: CRC Press).

Felleman, D.J., and Van Essen, D.C. (1991). Distributed hierarchical processing in the primate cerebral cortex. Cereb. Cortex *1*, 1–47.

Fries, P. (2005). A mechanism for cognitive dynamics: neuronal communication through neuronal coherence. Trends Cogn. Sci. *9*, 474–480.

Fries, P. (2009). The model- and the data-gamma. Neuron *64*, 601–602.

Friston, K. (2008). Hierarchical models in the brain. PLoS Comput. Biol. *4*, e1000211.

Gregoriou, G.G., Gotts, S.J., Zhou, H., and Desimone, R. (2009). High-frequency, long-range coupling between prefrontal and visual cortex during attention. Science *324*, 1207–1210.

Hasenstaub, A., Shu, Y., Haider, B., Kraushaar, U., Duque, A., and McCormick, D.A. (2005). Inhibitory postsynaptic potentials carry synchronized frequency information in active cortical networks. Neuron *47*, 423–435.

Lamme, V.A., and Roelfsema, P.R. (2000). The distinct modes of vision offered by feedforward and recurrent processing. Trends Neurosci. *23*, 571–579.

Lee, J.H., Whittington, M.A., and Kopell, N.J. (2013). Top-down beta rhythms support selective attention via interlaminar interaction: a model. PLoS Comput. Biol. *9*, e1003164.

Markov, N.T., Misery, P., Falchier, A., Lamy, C., Vezoli, J., Quilodran, R., Gariel, M.A., Giroud, P., Ercsey-Ravasz, M., Pilaz, L.J., et al. (2011). Weight consistency specifies regularities of macaque cortical networks. Cereb. Cortex *21*, 1254–1272.

Markov, N.T., Ercsey-Ravasz, M.M., Ribeiro Gomes, A.R., Lamy, C., Magrou, L., Vezoli, J., Misery, P., Falchier, A., Quilodran, R., Gariel, M.A., et al. (2014a). A weighted and directed interareal connectivity matrix for macaque cerebral cortex. Cereb. Cortex *24*, 17–36.

Markov, N.T., Vezoli, J., Chameau, P., Falchier, A., Quilodran, R., Huissoud, C., Lamy, C., Misery, P., Giroud, P., Ullman, S., et al. (2014b). Anatomy of hierarchy: feedforward and feedback pathways in macaque visual cortex. J. Comp. Neurol. *522*, 225–259.

Mesulam, M.M. (1998). From sensation to cognition. Brain *121*, 1013–1052.

Mitra, P.P., and Pesaran, B. (1999). Analysis of dynamic brain imaging data. Biophys. J. *76*, 691–708.

Moran, J., and Desimone, R. (1985). Selective attention gates visual processing in the extrastriate cortex. Science *229*, 782–784.

Nalatore, H., Ding, M., and Rangarajan, G. (2007). Mitigating the effects of measurement noise on Granger causality. Phys. Rev. E Stat. Nonlin. Soft Matter Phys. *75*, 031123.

Niessing, J., Ebisch, B., Schmidt, K.E., Niessing, M., Singer, W., and Galuske, R.A. (2005). Hemodynamic signals correlate tightly with synchronized gamma oscillations. Science *309*, 948–951.

Oostenveld, R., Fries, P., Maris, E., and Schoffelen, J.M. (2011). FieldTrip: Open source software for advanced analysis of MEG, EEG, and invasive electrophysiological data. Comput. Intell. Neurosci. *2011*, 156869.

Paxinos, G., Huang, X., and Toga, A.W. (1999). The Rhesus Monkey Brain in Stereotaxic Coordinates. (Waltham, Mass.: Academic Press).

Posner, M.I., Snyder, C.R., and Davidson, B.J. (1980). Attention and the detection of signals. J. Exp. Psychol. *109*, 160–174.

Raffi, M., and Siegel, R.M. (2005). Functional architecture of spatial attention in the parietal cortex of the behaving monkey. J. Neurosci. *25*, 5171–5186.

Rawley, J.B., and Constantinidis, C. (2010). Effects of task and coordinate frame of attention in area 7a of the primate posterior parietal cortex. J. Vision *10*, 11–16.

Roberts, M.J., Lowet, E., Brunet, N.M., Ter Wal, M., Tiesinga, P., Fries, P., and De Weerd, P. (2013). Robust gamma coherence between macaque V1 and V2 by dynamic frequency matching. Neuron *78*, 523–536.

Rubehn, B., Bosman, C., Oostenveld, R., Fries, P., and Stieglitz, T. (2009). A MEMS-based flexible multichannel ECoG-electrode array. J. Neural Eng. *6*, 036003.

Salazar, R.F., Dotson, N.M., Bressler, S.L., and Gray, C.M. (2012). Content-specific fronto-parietal synchronization during visual working memory. Science *338*, 1097–1100.

Saleem, K.S., and Logothetis, N.K. (2007). A Combined MRI and Histology Atlas of the Rhesus Monkey Brain in Stereotaxic Coordinates. (Waltham, Mass.: Academic Press).

Siegel, M., Donner, T.H., Oostenveld, R., Fries, P., and Engel, A.K. (2008). Neuronal synchronization along the dorsal visual pathway reflects the focus of spatial attention. Neuron *60*, 709–719.

Tallon-Baudry, C., Bertrand, O., and Fischer, C. (2001). Oscillatory synchrony between human extrastriate areas during visual short-term memory maintenance. J. Neurosci. *21*, RC177.

Van Essen, D.C. (2012). Cortical cartography and Caret software. Neuroimage *62*, 757–764.

van Kerkoerle, T., Self, M.W., Dagnino, B., Gariel-Mathis, M.A., Poort, J., van der Togt, C., and Roelfsema, P.R. (2014). Alpha and gamma oscillations characterize feedback and feedforward processing in monkey visual cortex. Proc. Natl. Acad. Sci. USA *111*, 14332–14341.

von Stein, A., Chiang, C., and König, P. (2000). Top-down processing mediated by interareal synchronization. Proc. Natl. Acad. Sci. USA *97*, 14748–14753.

Wang, X.J. (2010). Neurophysiological and computational principles of cortical rhythms in cognition. Physiol. Rev. *90*, 1195–1268.

Watanabe, H., Sato, M.A., Suzuki, T., Nambu, A., Nishimura, Y., Kawato, M., and Isa, T. (2012). Reconstruction of movement-related intracortical activity from micro-electrocorticogram array signals in monkey primary motor cortex. J. Neural Eng. *9*, 036006.

Wen, X., Rangarajan, G., and Ding, M. (2013). Multivariate Granger causality: an estimation framework based on factorization of the spectral density matrix. Philos. Trans. A Math. Phys. Eng. Sci. *371*, 20110610.

Womelsdorf, T., Schoffelen, J.M., Oostenveld, R., Singer, W., Desimone, R., Engel, A.K., and Fries, P. (2007). Modulation of neuronal interactions through neuronal synchronization. Science *316*, 1609–1612.

Xing, D., Yeh, C.I., Burns, S., and Shapley, R.M. (2012). Laminar analysis of visually evoked activity in the primary visual cortex. Proc. Natl. Acad. Sci. USA *109*, 13871–13876.